
Article:
Darbar, Y., Isamail, S.A., Sykes, T. et al. (Accepted: 2026) Role of diffusion in mixing in inkjet printed droplets. Physical Review Fluids. ISSN: 2469-990X (In Press)

The Role of Diffusion in Mixing Inkjet Printed Droplets

Yatin Darbar*
Centre for Doctoral Training in Fluid Dynamics, University of Leeds, Leeds, LS2 9JT, United Kingdom

Ahmed Said Ismail
School of Engineering and Materials Science, Queen Mary Universtiy London, London, E1 4NS, United Kingdom

Thomas C. Sykes
Department of Engineering Science, University of Oxford, Oxford OX1 3PJ, United Kingdom and
School of Engineering, University of Warwick, Coventry CV4 7AL, United Kingdom

David Harbottle
School of Chemical and Process Engineering, University of Leeds, Leeds, LS2 9JT, United Kingdom

Harvey M. Thompson and Mark C. T. Wilson†
School of Mechanical Engineering, University of Leeds, Leeds, LS2 9JT, United Kingdom

The mixing dynamics of a coalescing sessile and impacting liquid droplet on a solid surface is studied numerically. The numerical simulations utilise the volume of fluid method coupled with an advection-diffusion equation to assess diffusive mixing within the droplets. The simulation methods are extensively validated against analytical and experimental results confirming their ability to capture diffusion in droplet systems. Using dimensions and properties relevant to inkjet printing systems, the time scale for droplet mixing in printing and other microfluidic applications that concern the impact and coalescence of droplets is determined. Results show little mixing occurs during the impact and relaxation of the printed droplets, with complete homogenisation driven mainly by molecular diffusion over a much longer times scale than the impact. The effects of key printing parameters, including droplet size, printing separation and substrate wettability are explored to quantify their impact on droplet mixing times. Understanding the effect of these parameters on the time scale for droplet mixing gives potential avenues to enhance or suppress droplet mixing before the mechanisms of evaporation or curing become relevant.

* yatin˙darbar@hotmail.co.uk
† M.Wilson@leeds.ac.uk

I. INTRODUCTION

The dynamics of impacting and coalescing droplets on a solid surface is important in inkjet printing applications such as, the fabrication of biological materials and functional electronics [1, 2], as well as more established fields like microfluidics, chemical synthesis, and rapid prototyping [3–5]. As a result, the physics governing droplet impact and coalescence is of major practical, as well as fundamental interest. Reviews such as those of Yarin [6] or Josserand and Thoroddsen [7] show that the Reynolds number, $Re = \rho U R/\mu$, where ρ is the fluid density, U is the droplet impact velocity and R is the droplet radius combined with the Weber number, $We = \rho U^2 R/\sigma$, where σ is the surface tension, are key to characterising the outcomes of droplet impact and coalescence on a surface.

Early studies on inkjet printing focused mainly on the free surface and wetting dynamics of the deposited droplets. Menchaca-Rocha *et al.* [8], for example, used high-speed imaging to study the coalescence of two sessile mercury droplets and compare the evolution of the meniscus bridge to theoretical models. This work was extended by Pawar *et al.* [9], who used both high speed imaging and lattice Boltzmann simulations to study coalescence of sessile droplets of varying sizes, and by Li *et al.* [10] who studied experimentally the impact of a falling droplet onto a stationary sessile droplet. Due to its industrial significance these studies focused on the spread length of the combined droplet under varying impact speeds and droplet offsets.

The internal dynamics of droplets are of critical importance in applications where mixing between fluid phases or reagents is essential [11]. Despite this, only a limited number of studies have examined the internal and mixing dynamics of printed droplets on a solid surface.

Fundamental studies commonly use a configuration that involves the impact of a droplet onto a sessile droplet. Castrejon-Pita *et al.* [12] experimentally studied this system using particle image velocimetry (PIV) within millimetre-sized droplets to examine the internal velocity field of impacting and coalescing droplets. Further to this, some studies have considered how a wettability-gradient on the substrate can enhance the internal mixing of coalescing sessile droplets by inducing jet-like horizontal, recirculating flows [13, 14].

Application-driven studies by Kröber *et al.* [15] and Fathi and Dickens [16] used fluorescent dyes and confocal laser scanning microscopy to assess the chemical synthesis of polyuthethane and nylon 6 respectively. Both investigations conclude that good mixing occurs during drop-on-drop deposition of reactive fluids as no concentration gradients of the fluorescent dye could be seen, with unmixed areas being confined to near the contact line. However, in both studies the system was viewed from directly above, hence the three-dimensional reaction or mixing dynamics could not be observed.

Building on earlier work, Castrejón-Pita *et al.* [17] used high-speed PIV and lattice Boltzmann simulations to analyse the internal dynamics of an undyed sessile droplet and a dyed impacting droplet. This study used millimeter-scale droplets with their dynamics matched to inkjet conditions through the Reynolds and Weber numbers. Limited mixing between the droplets was reported due to minimal advection of the internal interface between the dyed and undyed fluid regions. However, the relative importance of diffusion in this study was not matched to inkjet conditions, suggesting that diffusion may play a more significant role during coalescence at the scale of inkjet printing. The direct internal and mixing dynamics of inkjet printed droplets remains inaccessible experimentally due to the high temporal and spatial resolutions needed [18].

An alternative approach that can provide further insight into microscale droplet dynamics is to use numerical simulations. There are a number of numerical methods for the effective modelling of free surface flows that can be applied to a study of droplets [19]. Extensive numerical tools have been developed to study and optimise mixing in droplets confined within microfluidic channels [20, 21]. These however, do not translate well to the open-air, free-surface configurations found in inkjet printing. Recent work using Volume of Fluid (VOF) methods has captured substrate effects and internal flow structures. Sykes *et al.* [22] made progress in modelling these unconfined systems by using a Volume of Fluid (VOF) method combined with the Kistler dynamic contact angle model to incorporate substrate wettability. Their simulations revealed the formation of internal jets during coalescence, driven by capillary waves reflecting off the contact line, and demonstrated how jet strength depends strongly on the receding contact angle. These results supported prior experimental observations showing that substrate wettability significantly influences mixing. However, their approach tracked only advective transport within the droplets, without accounting for molecular diffusion.

Alternatively, Yi *et al.* [23] applied a Many-Body Dissipative Particle Dynamics (MDPD) method to simulate the impingement of micrometer-scale droplets. Their model inherently included diffusive mixing due to its molecular dynamics origin, and they reported that non-wetting conditions led to enhanced mixing. However, the results suggested a potential overestimation of diffusive contributions. As such, a research gap remains in the modeling of both advection and molecular diffusion under physically realistic inkjet conditions, where droplet-scale mixing governs critical process outcomes.

In this study, we present a numerical framework capable of capturing real-material diffusion in coalescing droplet systems using an extended Volume of Fluid method implemented in OpenFOAM [24, 25]. The model is validated

comprehensively against analytical and experimental benchmarks, and applied to inkjet-scale droplet collisions where mixing is dominated by molecular diffusion. We systematically quantify the influence of droplet spacing, size, volume ratio and substrate wettability on the time required to reach a given level of mixing. Building on these results, we propose a generalised scaling law that predicts mixing time as a function of lateral separation and threshold concentration. This work provides a physically grounded, computationally accessible approach for understanding and optimizing diffusive mixing in reactive inkjet and other droplet-based technologies.

II. NUMERICAL SIMULATION METHOD

Simulations were performed using a custom-built numerical framework developed within OpenFOAM [26]. The `interFoam` solver was coupled with the `phaseScalarTransport` library in order to model real material diffusion in a multiphase system. This framework couples the Volume of Fluid (VOF) method for modelling multiphase flow with an advection-diffusion equation of a scalar concentration field. Therefore, the model captures both the external dynamics of droplet impact and coalescence and the internal evolution of concentration fields, enabling assessment of mixing.

A. Hydrodynamic Model

The VOF method is a one-fluid model that uses a conserved volume fraction $\alpha \in [0, 1]$, to represent areas in the simulation domain corresponding to the droplets ($\alpha = 1$), surrounding air ($\alpha = 0$) and the droplet-air interface between them ($0 < \alpha < 1$). This method has been used by a number of previous authors and is well-suited to modeling droplet impact and coalescence [22, 27, 28]. The material parameters of the droplet and air are combined to define a mixture liquid with density ρ and viscosity μ, in which

$$\rho = \alpha\rho_d + (1 - \alpha)\rho_g, \tag{1}$$

$$\mu = \alpha\mu_d + (1 - \alpha)\mu_g, \tag{2}$$

where ρ_d, ρ_g, μ_d and μ_g are the densities and viscosities of the liquid droplet and air phases respectively. A single set of compressible Navier-Stokes equations are solved for the mixture fluid. The conservation of mass is given by

$$\frac{\partial \rho}{\partial t} + \nabla \cdot (\rho \mathbf{u}) = 0, \tag{3}$$

where $\mathbf{u}$ is the fluid velocity, while the equation for the conservation of momentum is

$$\frac{\partial}{\partial t}(\rho \mathbf{u}) + \nabla \cdot (\rho \mathbf{u}\mathbf{u}) = \nabla \cdot \mathbf{T} + \rho \mathbf{F} + \mathbf{F_s}, \tag{4}$$

where $\mathbf{T}$ is the stress tensor, $\mathbf{F}$ are the unit body forces and $\mathbf{F_s}$ represents the surface tension force. The fluids considered are Newtonian, therefore the stress tensor is given by

$$\mathbf{T} = -p\mathbf{I} + \mu \left(\nabla \mathbf{u} + \nabla \mathbf{u}^T \right), \tag{5}$$

where p is the pressure and $\mathbf{I}$ is the metric tensor of the coordinate frame. Surface tension is included by using the continuum surface force model of Brackbill *et al.* [29]. In this way surface tension is approximated as a body force near the free surface

$$\mathbf{F_s} = \sigma\kappa\nabla\alpha, \tag{6}$$

where σ the surface tension and κ the free surface curvature given by

$$\kappa = -\nabla \cdot \left(\frac{\nabla \alpha}{|\nabla \alpha|} \right). \tag{7}$$

For the systems considered here, the Bond Number $\mathrm{Bo} = \Delta\rho g R^2/\sigma \approx 5 \times 10^{-4}$, where g is acceleration due to gravity and $\Delta\rho$ is the difference in density between the droplet fluid and air, therefore the effects of gravity are neglected. A final equation, for the volume fraction α, is:

$$\frac{\partial \alpha}{\partial t} + \nabla \cdot (\alpha \mathbf{u}) + \nabla(\mathbf{u}_c \alpha(1 - \alpha)) = 0, \tag{8}$$

where $\mathbf{u}_c$ is an artificial compression velocity that limits the effects of numerical diffusion of the fluid-fluid interface [30, 31].

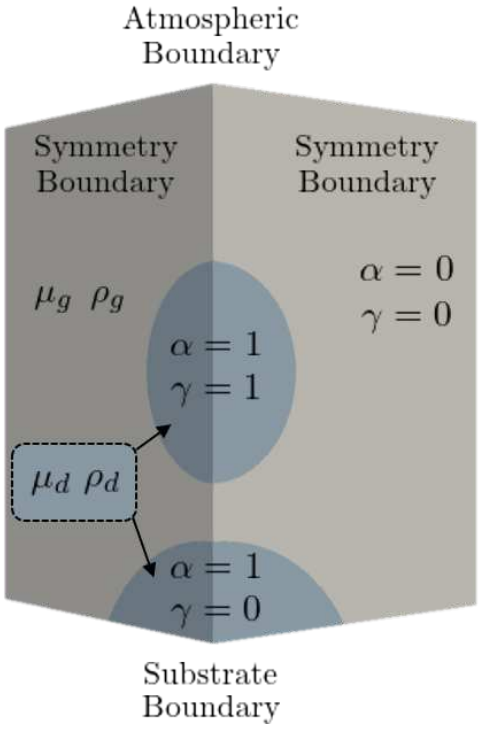

FIG. 1. Illustration of the three-dimensional quarter domain used in the simulation method. The droplet and gas material properties, the volume fraction and the diffusing scalar γ are labeled. The visible faces of the domain are identified, the other faces are atmospheric boundaries also.

B. Diffusion Model

To evaluate the mixing within the droplets an additional scalar γ, in which $\gamma = 1$ is initialised within the impacting droplet and $\gamma = 0$ throughout the rest of the computational domain. The transport of the scalar field is governed by the advection-diffusion equation

$$\frac{\partial}{\partial t}(\alpha\gamma) + \nabla \cdot (\alpha\gamma\mathbf{u}) = \nabla \cdot (D\alpha\nabla\gamma), \tag{9}$$

where D is the diffusivity of the scalar. Restriction of the scalar γ to only the droplet phase is achieved within the model by conserving the quantity $\alpha\gamma$ within (9). Note that since there is only a one-way coupling between γ and the velocity field, the former has no influence on the dynamics of the system. Conservation of the scalar γ is vital for the accuracy of capturing diffusion in the droplet systems, the conservation of the added scalar has been checked in a simulation representative of those studied throughout this work (See Appendix B).

C. Computational Domain & Mesh

To reduce computational expense, flow symmetry is exploited where possible. For axisymmetric systems, a three-dimensional quarter domain is used (See Figure 1). However, for impacts with a lateral separation between the droplets, simulations are preformed in a half domain. A base mesh of at least 10 cells per radius of the free impacting droplet (R_f) in the surrounding gas phase was used. Any cell that contained the droplet or interface ($\alpha > 0$) was marked for adaptive mesh refinement. Three levels of adaptive mesh refinement were performed on cells marked for refinement so that the mesh has a resolution of 80 cells per R_f in the droplet phase.

D. Boundary Conditions

On faces of the domain that represent planes of symmetry the normal velocity component across the symmetry plane is equal to zero. For scalar fields such as pressure, volume fraction and diffusing scalar a zero gradient condition

is enforced. On the faces of the domain that are opposite the symmetry and substrate planes, atmospheric boundary conditions are imposed. Here, the normal component of velocity, pressure and flux of the diffusive scalar are all set to zero. The volume fraction obeys zero Neumann and Dirichlet boundary conditions for outflow and inflow, respectively, which ensures that only air can enter the domain.

It is vital to model the fluid-solid interaction on the substrate accurately in order to produce the correct wetting dynamics. Following previous studies, [32–34], the empirical model of Kistler [35] is used. Kistler's model has previously been used successfully within the OpenFOAM framework, [22, 36, 37], where the dynamic contact angle θ is given by

$$\theta = f_H[Ca + f_H^{-1}(\Theta)], \tag{10}$$

and Ca is the contact line capillary number given by $Ca = \mu|u_{cl}|/\sigma$ (where μ is the droplet viscosity, u_{cl} the contact line velocity, σ the surface tension), and f_H is the Hoffman function. The latter is given by

$$f_H(s) = \arccos\left(1 - 2\tanh\left[5.16\left(\frac{s}{1+1.31s^{0.99}}\right)^{0.706}\right]\right). \tag{11}$$

The effects of contact angle hysteresis must also be considered for accurate modeling of the dynamics [12, 38]. These can be incorporated into Kistler's model through the dummy variable Θ in (11). Depending on the direction of the contact line (advancing, static, receding), the value of Θ is given by

$$\Theta = \begin{cases} \theta_A & \text{for } u_{cl}\cdot\hat{\mathbf{n}} > 0, \\ \theta_E & \text{for } u_{cl} = 0, \\ \theta_R & \text{for } u_{cl}\cdot\hat{\mathbf{n}} < 0 \end{cases} \tag{12}$$

where θ_A, θ_E and θ_R are prescribed (minimum) advancing, equilibrium and (maximum) receding contact angles, respectively and $\hat{\mathbf{n}}$ is the outward pointing unit normal to the free surface. By varying the values of θ_A, θ_E, θ_R independently, an accurate model of the substrate wettability can be obtained. In this study the values of θ_A, θ_E and θ_R are taken from the experimental data of Castrejón-Pita *et al.* [17]. Equation (10) is used as a boundary condition on the substrate for the volume fraction. In addition to this, a no-slip condition is applied to velocity, and a zero Neumann condition is enforced on the diffusing scalar γ. Finally the pressure boundary condition is chosen to be determined by the velocity. It is important to note that within the cell-centred finite-volume discretisation used, fluxes are evaluated over the entire control volume, so the velocity at the cell centre adjacent to the wall remains non-zero despite the prescribed no-slip condition at the cell face. This introduces a small but finite effective slip in the mesh cell closest to the wall, which avoids the classical shear-stress singularity.

E. Assessment of Mixing

The mixing dynamics of the droplets is investigated quantitatively using a mixing index. Following previous studies, a metric based upon the variance of the scalar field γ is used [21, 39, 40]:

$$M^*(t) = \sqrt{\int_{V_D} (\gamma(t) - \bar{\gamma}(t))^2 \, dV}, \tag{13}$$

To give a clear measure of the mixing within the droplets, the metric in (13) is normalised according to

$$M(t) = 1 - \frac{M^*(t)}{M(0)}. \tag{14}$$

Now, $M = 0$ corresponds to the droplets being completely unmixed, whereas $M = 1$ corresponds to the combined droplet being fully-mixed with a uniform value of γ throughout.

III. NUMERICAL VALIDATION

A. Experimental Validation of Droplet Impact and Coalescence Dynamics

The OpenFOAM simulation framework has been previously validated for accurately capturing capillary driven free surface flows [30]. In particular the external and advective mixing dynamics for the coalescence of a free droplet and

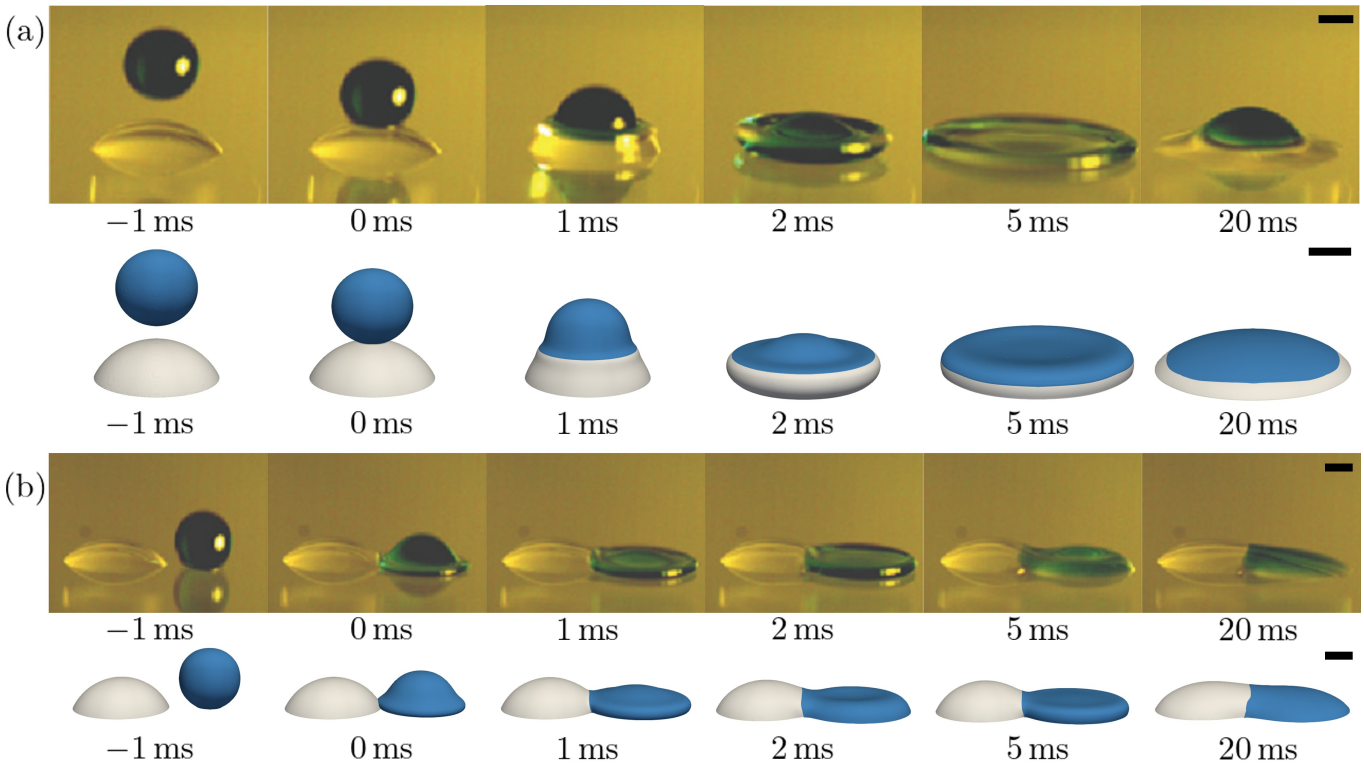

FIG. 2. Comparisons of the impact and relaxation dynamics between experiments [17] and simulations as a function of horizontal droplet separation. (a) 0 mm, (b) 4 mm, both cases have Re = 22.1 and We = 31.7. Scale bars are 1.39 mm. Experimental figures are reprinted with permission from Castrejón-Pita *et al.* [17]. Copyrighted by the American Physical Society.

a sessile droplet in air has been undertaken by Sykes *et al.* [22]. Here, to further validate the numerical simulation method, the impact and coalescence of a sessile and an impacting droplet on a solid surface are simulated and compared with the experiments of Castrejón-Pita *et al.* [17], shown in Figure 2. The focus of this is to ensure accurate simulations of the impact process, especially in non-axisymmetric configurations. The printed droplets have R =1.39 mm, ρ = 1220 kg m^{-3}, μ = 85.8 mPa s, σ = 67.1 mN m^{-1} and U = 1.12 m s^{-1}, corresponding to a dimensionless parameter regime Re = 22.1 and We = 31.7. The gas phase is taken to be air, with density 1.2 kg m^{-3} and viscosity 18 µPa s. In line with the experiments, the impacting droplet has been coloured and time $t = 0$ is taken as the moment of first contact between the droplets.

Figure 2(a) is a direct (drop-on-drop) collision of the droplets in which the centre of the impacting droplet lies directly above the centre of the sessile droplet. The impacting droplet has sufficient inertia to cause a large deformation to the combined droplet and flatten it causing spreading of the contact line across the substrate. When the combined droplet flattens there is significant stretching of the internal interface between the droplets, however no folding of this region occurs which would enhance mixing. Once the combined droplet has reached its maximum spread length it begins to recoil and the internal interface shrinks without significant mixing between the two droplets.

The second case presented in Figure 2(b) corresponds to a side-by-side deposition with a lateral offset of 4 mm. In this case, the falling droplet first impacts and spreads over the substrate before coalescing with the sessile droplet. When the droplets coalesce a meniscus bridge forms between the droplets increasing the internal interface between the droplets. This interface is driven towards the sessile droplet as the impacting droplet spreads over the substrate but again, no folding of the internal interface is observed. The combined droplet comes to rest in a non-spherical shape on the substrate due to the wettability of the substrate. Overall, the simulation method reproduces the experimental observations well.

B. Analytical Validation of Diffusion Model

The numerical model, given by (9), was first validated against a one-dimensional analytic test case, see Figure 3. A static square domain side length $2L$ was initialised with water occupying the lower half, with air above, forming

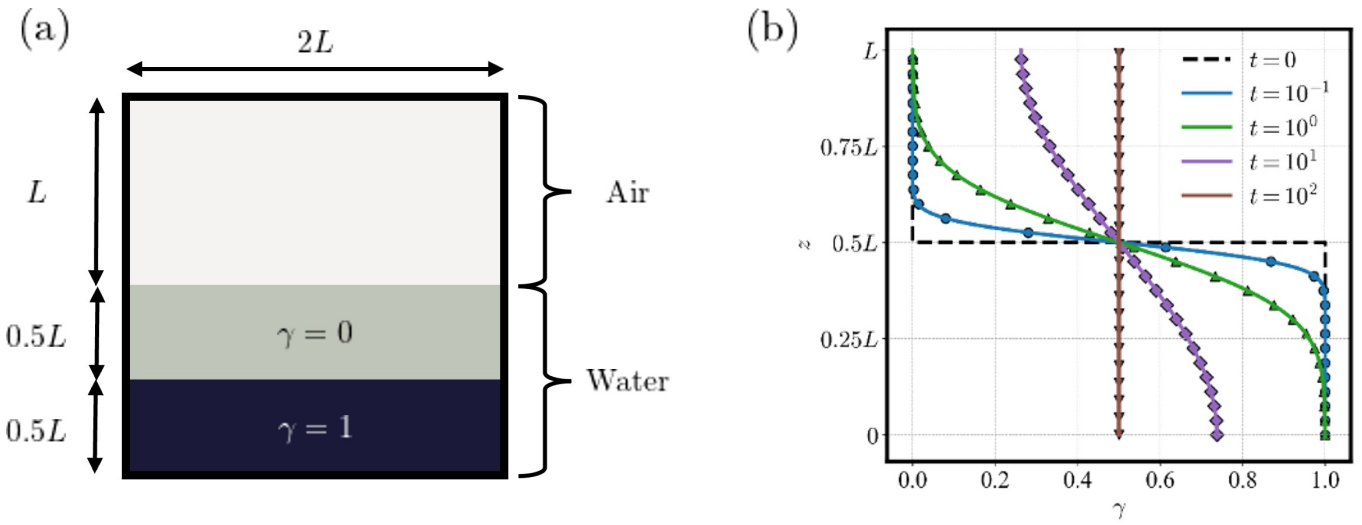

FIG. 3. Analytical validation of the numerical model. (a) Sketch of the test problem. (b) Quantitative comparison between concentrations predicted by the analytical (solid line) and numerical (marker) solutions.

a horizontal water-air interface at L. The diffusing scalar γ, was set to unity in the lower half of the water and zero elsewhere. With no flow or sources, transport of the scalar occurs solely in the vertical direction via diffusion, rendering the system one-dimensional. The concentration profile of γ can be found by solving

$$\gamma_t = D\gamma_{zz}, \quad z \in [0, L], \quad t > 0. \tag{15}$$

$$\gamma_z(0,t) = \gamma_z(L,t) = 0, \quad t > 0. \tag{16}$$

$$\gamma(z,0) = \gamma_0(z) = \begin{cases} 1 & \text{for } 0 < z < \frac{L}{2} \\ 0 & \text{for } \frac{L}{2} < z < L. \end{cases} \tag{17}$$

where z is the vertical coordinate of the domain, t is time and D is the diffusivity of the scalar γ. The solution can be obtained as the Fourier series

$$\gamma(z,t) = \frac{1}{2} + \sum_{n=1}^{\infty} \frac{2}{n\pi} \sin\left(\frac{n\pi}{2}\right) \cos\left(\frac{n\pi z}{L}\right) \exp\left(-\frac{n^2\pi^2 D}{L^2} t\right). \tag{18}$$

A comparison of the analytic and numerical concentration profiles is presented in Figure 3(b). The agreement is excellent and shows that the numerical solution preserves a zero flux of the scalar at the free surface ($z = L$) throughout the simulations, thereby limiting the scalar to the droplet phase.

C. Experimental Validation of Diffusion Model

The mixing of droplets attached to capillaries was investigated experimentally. Two 125 µm diameter droplets were grown at the ends of two capillaries and allowed to coalesce. Post-coalescence dynamics were recorded at 50 ms intervals, capturing the gradual migration of dye across the combined droplet. Figure 4 shows the experimental results. Due to the small length scales involved there was difficulty aligning the droplets which caused a slight vertical offset to the experimental system. To replicate the droplet-capillary experiment, two just-touching spherical droplets of diameter 125 µm were positioned to initiate coalescence. To mimic attachment to capillaries, each droplet intersected the domain boundary, truncating a chord length of 90 µm. Both droplets were modeled as pure water with properties matching experimental measurements density $\rho = 998\,\mathrm{kg\,m^{-3}}$, viscosity $\mu = 0.9\,\mathrm{mPa\,s}$, and surface tension $\sigma = 72.3\,\mathrm{mN\,m^{-1}}$. The dye diffusivity was taken to be 10^{-9} $\mathrm{m^2\,s^{-1}}$ which is a typical molecular diffusivity [41]. Figure 5 illustrates the evolution of the numerical simulation and gives a quantitative comparison of the numerical diffusion front (red) to the processed experimental front (gold). The diffusion front of the dye was extracted from

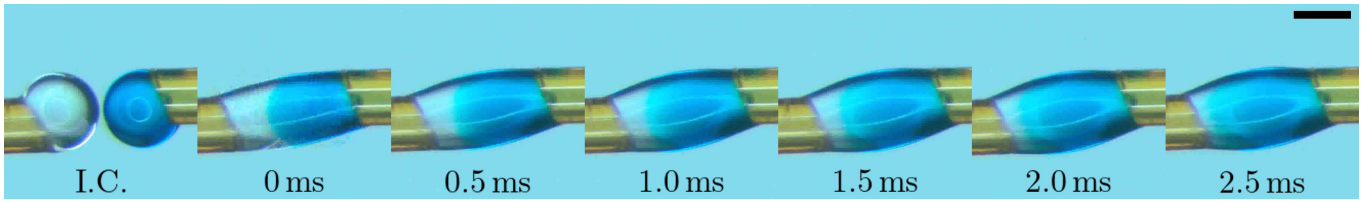

FIG. 4. Experimental images of the coalescence and mixing of droplets on capillaries. The blue dye introduced into the right hand droplet can be seen to diffuse to the left after coalescence has occurred. Scale bar is 90 µm

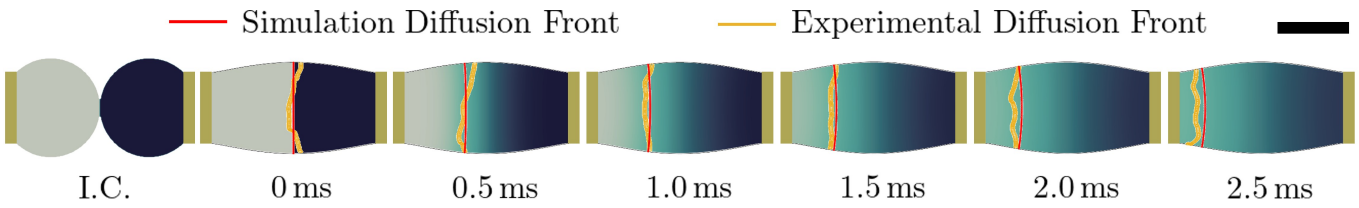

FIG. 5. Quantitative comparison of the numerical simulation of droplet mixing on capillaries. The predicted numerical simulation diffusion front (red) is compared to the image processed and experimental diffusion front (gold). Scale bar is 90 µm

the experimental images using the red channel of the RGB image to define a segmentation criterion. Since the exact concentration of the dye at this extracted diffusion front was unknown, a range of diffusion fronts from the simulations were compared to the experiments. It was found that the propagation of the contour $\gamma = 0.2$ matched the experimental data best. It is seen that the simulation results predict well the temporal evolution of the dye. The slight deviation may be due to the small vertical offset between the droplets in the experiments (due to alignment difficulties) which was not modeled in the simulations.

IV. RESULTS & DISCUSSION

To investigate the diffusive mixing dynamics of printed inkjet droplets the numerical simulation method was used to study the coalescence of an impacting droplet and a sessile droplet. The typical material properties for both droplets used in relevant applications are density $\rho \approx 1000\,\mathrm{kg\,m^{-3}}$, droplet radius $R \approx 50\,\mu\mathrm{m}$, impact velocity $U \approx 5\,\mathrm{m\,s^{-1}}$, viscosity $\mu \approx 10\,\mathrm{mPa\,s}$ and surface tension $\sigma \approx 45\,\mathrm{mN\,m^{-1}}$ [42]. Using these values gives rise to the following non-dimensional parameter regime, Re = 25, We = 28 and Bo $= 5.44 \times 10^{-4}$. Since Bo $<<$ 1, the effects of gravity are neglected. The Kistler contact angle model used $\theta_A = 70.0°$, $\theta_E = 63.2°$ and $\theta_R = 45.0°$ [17].

A. Mixing Dynamics of Inkjet Printed Droplets

Figure 6 shows the internal and external dynamics of an impacting and sessile droplet with Re = 25 and We = 28. The centre of the impacting droplet is directly above the centre of the sessile droplet resulting in an axisymmetric coalescence. The impacting droplet is initialised with a downward velocity of $5\,\mathrm{m\,s^{-1}}$ to recreate the printing process and the diffusing scalar ($\gamma = 1$) to assess mixing. Time $t = 0\,\mathrm{s}$ is taken to be the moment of first contact between the droplet.

After coalescence occurs, the meniscus bridge between the droplets expands radially as the inertia from the falling droplet drives it into the sessile droplet (5 µs). Blocked by the substrate, the downward momentum from the impact is diverted radially causing fluid to be forced outwards and the combined droplet begins to spread across the substrate (20 µs). Spreading causes the droplet to flatten out as fluid is sent towards the contact line and away from the centre and the typical pancake-type shape is formed. At this point the diffusing scalar added to the impacting droplet now covers the full extent of the combined droplet. After 50 µs, the inertia associated with the impact of the droplet has been lost due to viscous dissipation, now surface tension acts to retract the droplet. The recoil occurs over a much longer timescale than the dynamics associated with the impact. From 50 µs to 200 µs, due to the relatively high viscosity of the droplets and, hysteresis of the substrate, the contact lines only recede slightly.

Consistent with the findings of Castrejón-Pita *et al.* [17], only a small amount of mixing is observed on this timescale. By 200 µs the combined droplet has a stratified composition with the diffusing scalar occupying the upper half of the

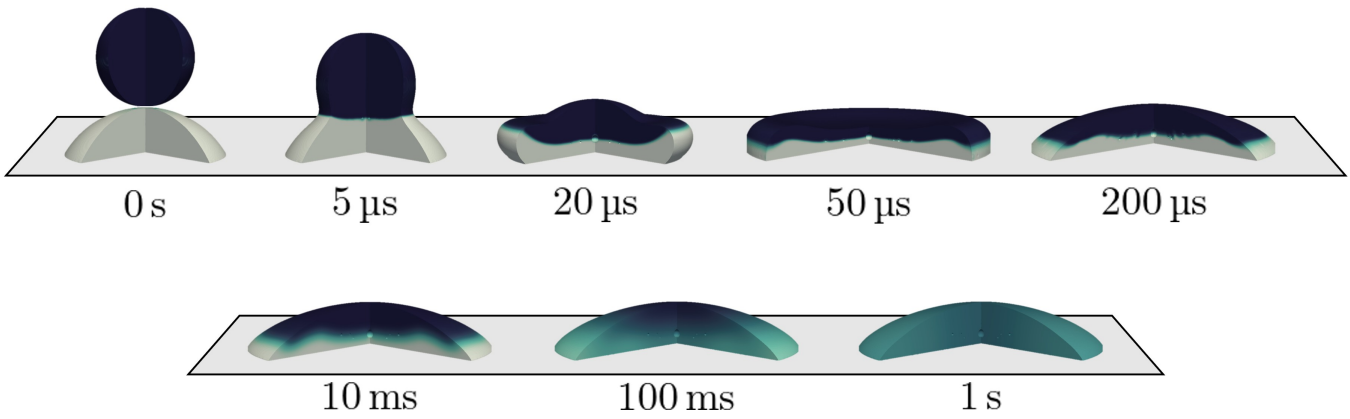

FIG. 6. Internal and external dynamics of an axisymmetric coalescence between a dyed impacting and undyed sessile droplet. Re = 25 and We = 28. During the impact and recoil little mixing occurs, hence diffusion acts over much longer time scale to homogenise the combined droplet.

droplet domain. It was proposed by Wilson *et al.* [41] that considerable diffusive mixing could occur during the time in which the combined droplet is elongated (50 µs in Figure 6). However, the simulation shows that this is not the case and no substantial migration of the diffusing species can be seen during the spread and recoil of the droplet. Further to this, no considerable stretching and folding of the internal fluid in the droplet has occurred to achieve good mixing by the time the static equilibrium is reached (≈ 200 µs). The droplet was deemed to reach a static equilibrium by measuring the kinetic energy of the droplet and free surface (See Appendix C). After this, material diffusion must act in order to completely homogenise the internal composition of the droplet.

From 10 ms – 100 ms the effects of diffusion can be observed as it begins to even out the high concentration gradient located in the middle of the droplet. This is an extremely slow mixing process, which further slows down as the magnitude of the concentration gradient diminishes. As the droplet mixes, the regions close to the top of the droplet and the contact line are the least well mixed due to their distance from the internal interface. Overall it takes between 1 s-3 s for the combined droplet to reach a uniform composition.

Figure 7 shows the mixing index as a function of time for the simulation presented in Figure 6, with an indication of the relationship between the internal composition and the mixing index. This analysis allows for the quantitative assessment of mixing within the droplet. This insight shows that, by the time the combined droplet has reached a static equilibrium (≈ 200 µs), it is less than 10% mixed. After this, the initially high concentration gradient of the diffusing scalar results in relatively fast (in diffusive terms) mixing over the first 0.1 s. In this time diffusive transport results in the droplet becoming nearly 60% mixed. As the magnitude of the concentration gradient decreases, the rate of mixing decreases as time evolves. By 0.5 s, only the extremities of the droplet remain less well mixed. As the rate of mixing has now reduced significantly it takes a further 2.5 s for the droplet to go from 80% (at 0.5 s) to 99% mixed (achieved at 2.95 s). Hence, the effect of diffusion to mix the droplet on the timescale of the coalescence is not as prominent as suggested in the literature [23]. Here the time scale for mixing of inkjet printed droplets is shown to be in the order of seconds. The visualisations is Figure 7 contain small structures within the droplet. These correspond to numerically predicted entrapped micro air bubbles that form during the rapid coalescence and impact stages. Their occurrence persisted across all mesh resolutions tested, suggesting that they are not mesh-dependent artefacts. Although their detailed dynamics are not the primary focus of this work, their presence is physically reasonable based on previous droplet impact studies [7].

To contextualise the results on diffusion-driven mixing, it is essential to consider the competing timescale of droplet evaporation. For inkjet-scale sessile droplets, both theoretical models and experimental studies consistently estimate evaporation times on the order of seconds under ambient, isothermal conditions [43, 44]. Applying the classical vapor diffusion model, the evaporation time can be approximated by

$$t_{\text{evap}} \approx \frac{\rho R_{\text{cl}}^2}{\mathcal{D}(C_{sat} - C_{\infty})}, \tag{19}$$

where R_{cl} is the contact line radius of the sessile droplet, $\mathcal{D}$ is the vapour diffusion coefficient of the fluid, and, C_{sat} and C_{∞} are the saturated vapour concentration and ambient atmosphere concentration respectively. For fluids with

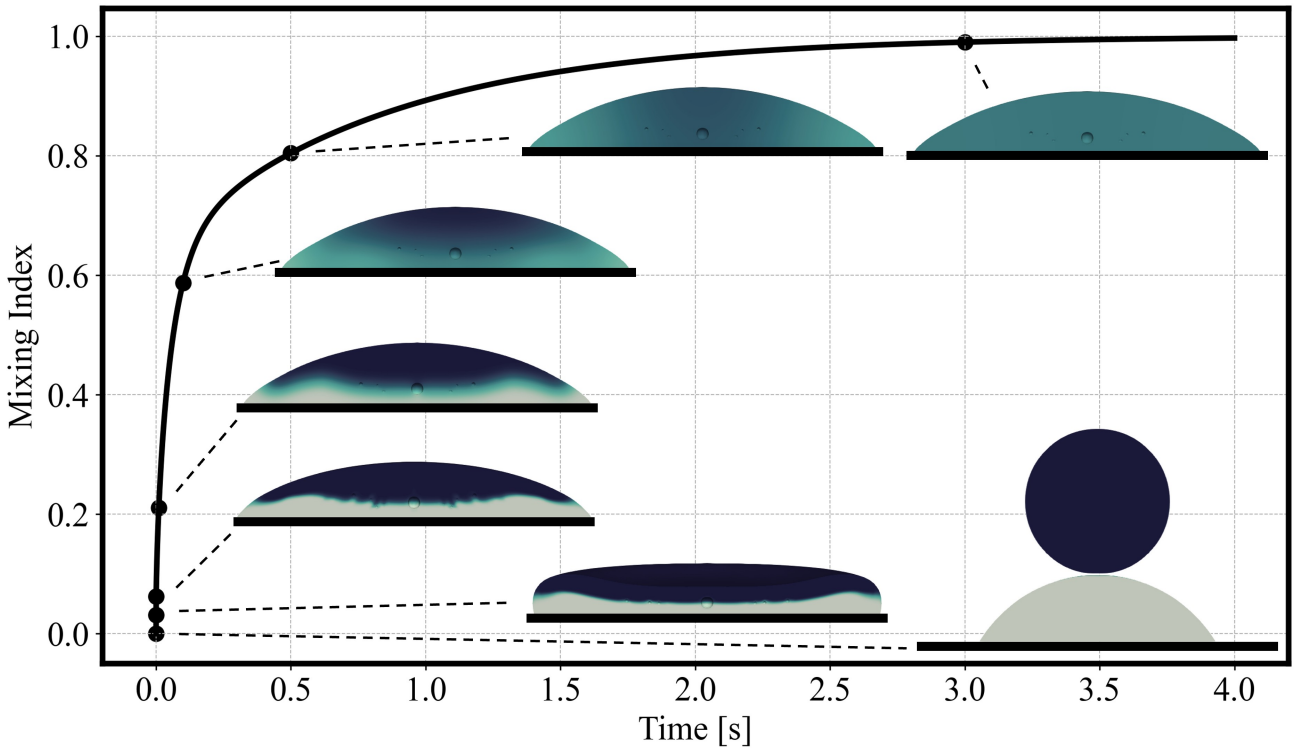

FIG. 7. Evolution of the mixing index with time for the simulation presented in Figure 6. Cross sections of the droplet are provided to give a visual representation of the mixed state of the combined droplet at a given mixing index value.

physical properties similar to those studied here (e.g., glycerol-water inks), this yields $t_{\text{evap}} \approx 10\,\text{s}$. This implies that diffusion within the droplet, which occurs over hundreds of milliseconds to a few seconds, will largely complete before evaporation effects become significant. Although the predicted mixing time (0.1 s -1 s) is considerably shorter than the evaporation timescale, these two processes are not fully decoupled. Local evaporation can alter concentration gradients and significantly influence the mixing dynamics. While evaporation can be accelerated via heated substrates which would strongly couple mixing and evaporation by reducing droplet lifetimes to below one second [45], the present study treats evaporation as negligible within the primary mixing window.

B. Effect of Droplet Size

Figure 8 shows a series of simulations in which the size of the printed droplets is decreased. A key advantage of inkjet printing is its ability to deliver small volumes of liquid in precise locations. For this reason it has surpassed traditional printing methods (e.g. screen printing) with its ability to print at resolutions less than 20 µm [46].

As the droplet size decreases, the Reynolds and Weber numbers of the system both decrease. Therefore the effect of viscosity and surface tension increase and the impact inertia decreases. The simulations show that, as the droplet size decreases, the impact has a less pronounced effect on the sessile droplet. As the droplet size decreases, the sessile droplet no longer spreads across the substrate but rather catches the impacting droplet. Hence, for smaller scales, the combined droplet has a much smaller spread length, with the internal interface located relatively higher above the substrate than for the larger droplet cases.

The mixing index data from the droplet size investigation simulations is presented in Figure 9(a). Smaller droplets mix quicker than larger ones owing the greater influence of diffusion in smaller systems. Figure 9(b) shows the droplet radius plotted against the time taken to reach $M = 0.99$ on a log-log scale. Analysis of this data shows that a line

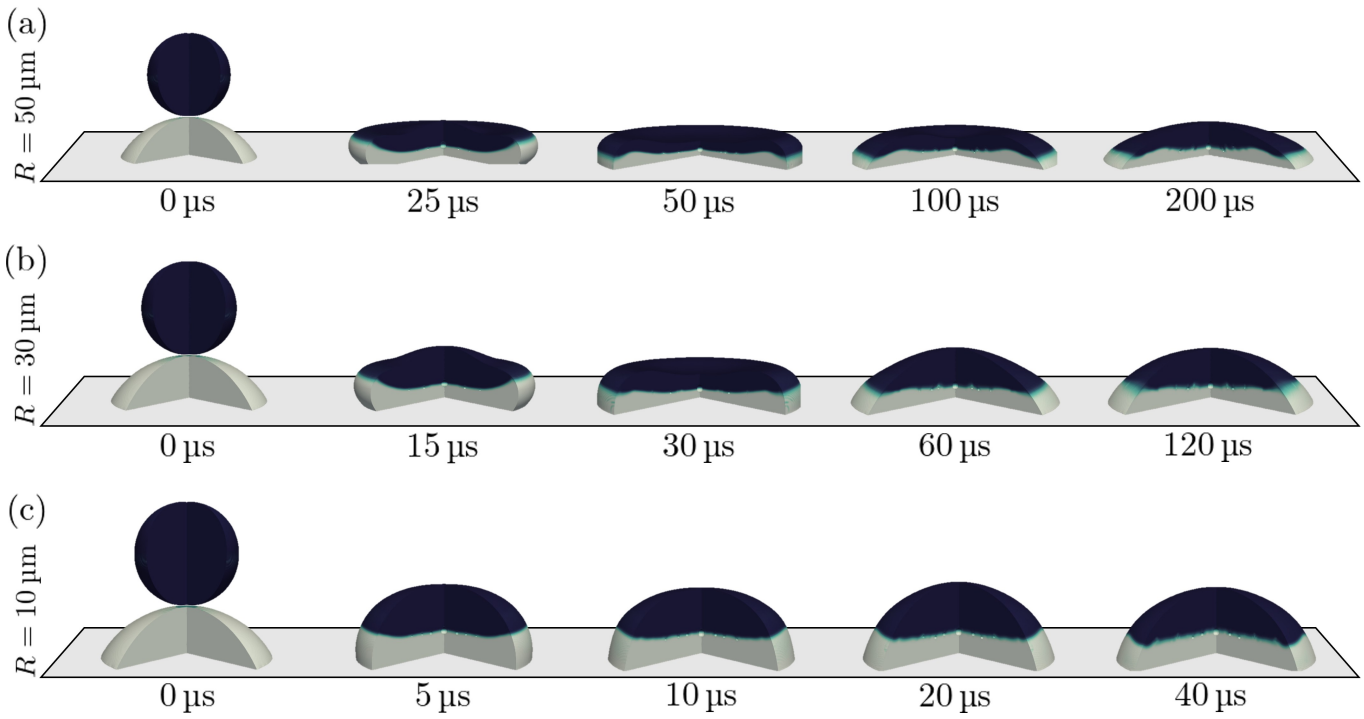

FIG. 8. The dynamics of axisymmetric printed droplets with droplets (a) $R = 50\,\mu m$ (Re = 25 and We = 28), (b) $R = 30\,\mu m$ (Re = 15 and We = 17) and (c) $R = 10\,\mu m$ (Re = 5 and We = 6).

of best fit through these points has a gradient 2.17. A simple empirical relationship such as this, within its range of applicability indicates that the time for inkjet printed droplets to fully mix scales closely to the square of the droplet radius (i.e. $T \propto R^2$).

C. Effect of Lateral Separation

In many applications the formation of three dimensional structures or surface patterning is desired. This calls for the non-axisymmetric deposition of droplets. To systematically explore offset depositions a lateral separation, S, is defined as the normalised distance between the centres of the impacting and sessile droplet measured along the plane parallel to the substrate. The free droplet radius $R = 50\,\mu m$ is used to normalise this parameter.

There are two critical values of the separation parameter. For small values of S, the impacting droplet first strikes the sessile droplet. In this case coalescence occurs, and then the combined droplet spreads across the substrate. As the separation increases, there exists an S^* such that the impacting droplet strikes the substrate before the sessile droplet. Modelling the droplets as solid bodies the critical separation S^* in this study is calculated to be $S^* = 1.62$. For lateral separations greater than this value the impacting droplet first spreads over the substrate and into the sessile droplet, initiating coalescence.

The second critical value of the lateral separation parameter is the maximum separation $S_{\max}$. As the printing separation increases, there exists a point in which the impacting droplet no longer has enough inertia to spread out and initiate coalescence. At this separation and beyond no mixing between the droplets would occur. Using models for the maximum spread diameter for a droplet impacting a solid surface from the literature [47–52], the maximum separation for this system can be estimated as $S_{\max} \approx 3.25$.

Figure 10 shows the simulation results for five lateral separations. Slices of the simulation have been taken in the vertical plane of symmetry in order to elucidate the internal composition of the droplet as well as the free surface dynamics. For non-zero separations less than S^* (Figures 10(b) and 10(c)), the impacting droplet hits the side of the sessile droplet as it travels towards the substrate. For brevity this regime will be called the *coalescence-spread* regime. Rather than flatten the sessile droplet as in the axisymmetric case, the impact causes fluid from the sessile droplet to be driven away from the impacting droplet. Because of this, fluid from the sessile droplet starts to spread away from the impacting droplet. At the same time, fluid in the impacting droplet also spreads across the substrate as the momentum of the droplet is re-directed outwards due to the presence of the substrate. As with the axisymmetric

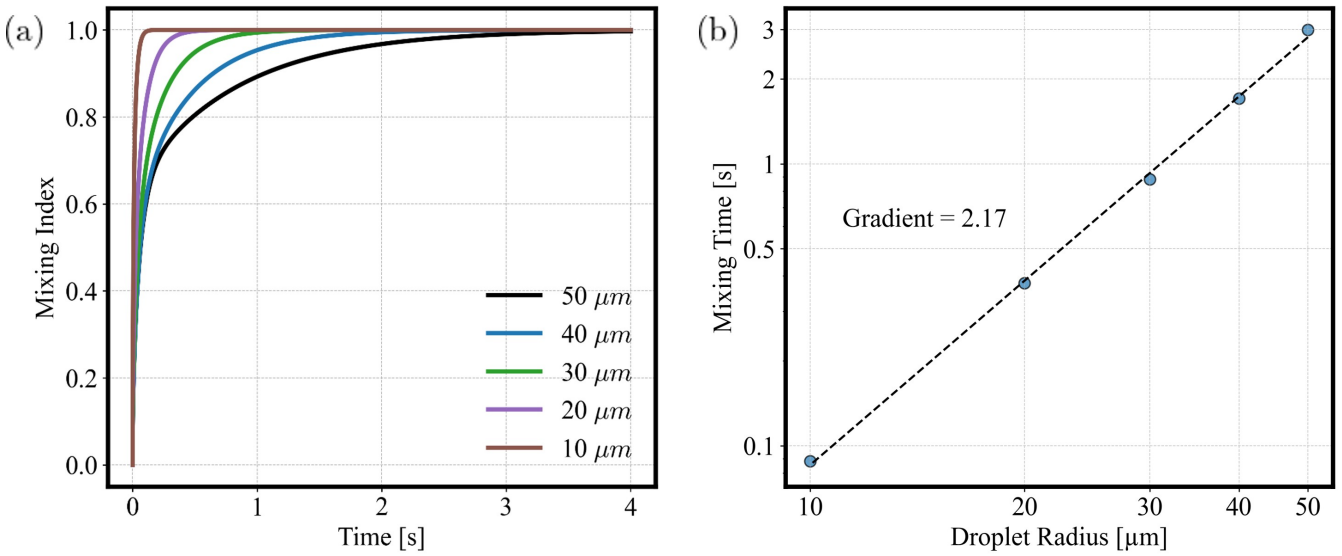

FIG. 9. Mixing data for all of the simulations conducted in the droplet size investigation. (a) Mixing index plotted against time. The self similar shape suggest a relationship between mixing and droplet size. (b) Mixing time plotted against droplet radius on a logarithmic scale on both axes. The gradient of the line of best fit through the data points shows that mixing time, $T \propto R^{2.17}$ for inkjet printed drops close to theory.

case, once the combined droplet has reach its maximum spread state, the contact line only recedes marginally as the effects of surface tension brings fluid back to the centre of the droplet. In this system, the large amount of viscous dissipation means there is little inertia after impact to cause a retraction of the droplet. The final sessile droplet in all cases is not a spherical cap, but a lens shape due to the effects of contact angle hysteresis [12].

For separations larger than S^* (Figure 10(d)), the printed droplet impacts the substrate before spreading into the sessile droplet and coalescing. Hence this regime will be denoted the *spread-coalescence* regime. The impacting droplet flattens substantially on the substrate and the fluid that spreads towards the sessile droplet initiates coalescence. In these cases the inertia from the impact is only enough to cause minor free surface deformations of the sessile droplet fluid close to the point of coalescence and the left contact line remains stationary.

By 300 µs, the combined droplets in all simulations have reached a static equilibrium. For all separations, the internal interface of the diffusing scalar is not folded over, with distinct areas of separation. Further to this, as the lateral separation increases, the length of the internal interface decreases. For $S = 0$ the internal interface is approximately horizontal spanning the width of the droplet, whereas for $S = 2.80$ the interface is vertically aligned covering the height of the droplet. The effect of this can be seen in the droplets at 0.1 s. With a smaller effective distance to work over and a larger internal interface to work across, diffusion mixes the droplets with a smaller separation much more quickly. By 1 s, the droplets printed with a small separation appear to have a qualitatively homogenous composition, the droplets that were printed with a larger separation however, have a distinct horizontal concentration gradient. It takes around an order of magnitude longer for the droplets printed at the highest separation to achieve the same qualitative homogeneous composition as the droplets printed directly on top of each other.

Evaluating the time required for droplets to reach various stages of mixing provides valuable insight into both the process and timescale of droplet mixing. As illustrated in Figure 11, the relationship between mixing percentage, separation and mixing time is non-linear as higher levels of mixing require disproportionately longer amounts of time. Achieving 99% mixing takes significantly longer than reaching lower thresholds (approximately double the time needed to achieve a 90% mixing). Considering the effects of evaporation, most simulated cases (except the largest droplet separation) reach at least 90% mixing before evaporation becomes significant (≈ 10 s). Using a more stringent 99% threshold results in only cases close to axisymmetric depositions achieve a well-mixed state in this time.

Figure 11 presents an empirical line of best fit for the mixing time as a function of separation for the 99% mixed data set. The method of determining these empirical trends and associated fitting parameters is given in Appendix D. Overall, the empirical trend show strong agreement with the simulation data, capturing the general trends well. In the coalescence–spread regime, the relationship between separation and mixing time exponentially decreasing. This indicates that perturbations to small printing separations have a larger increase on the mixing time than perturbations to intermediate separations. In contrast, the spread–coalescence regime displays a more consistent exponentially

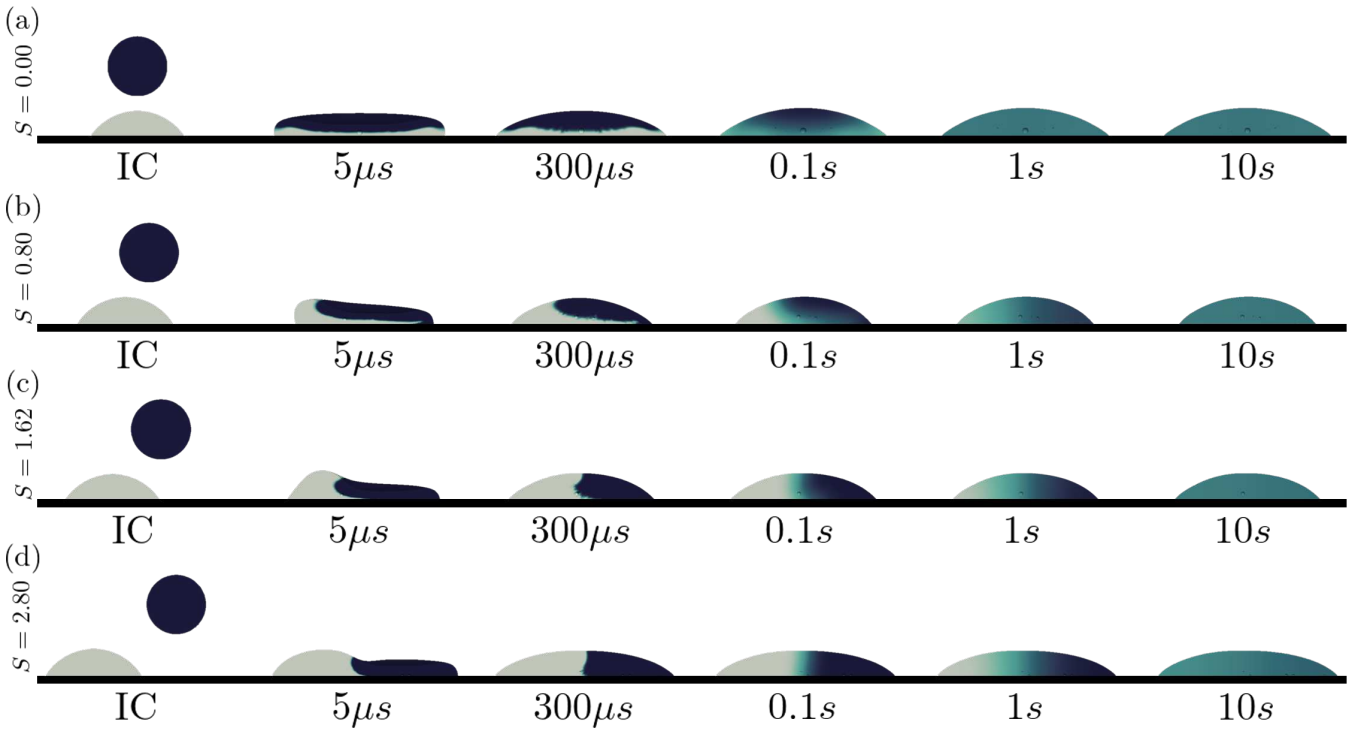

FIG. 10. Simulations of the internal and external dynamics of the impact and coalescence of an impacting droplet and a sessile droplet for different droplet separations. Re = 25 and We = 28.

increasing relationship between separation and mixing time. Nevertheless, as the mixing threshold increases, the gradient of this relationship also steepens, further indicating that greater separations require disproportionately more time to reach higher levels of mixing.

From the lines of best fit, an upper bound for the time T_M needed for a pair of inkjet droplets printed with a lateral separation S to be mixed via diffusion can be expressed as

$$T_M = \begin{cases} A_1 \times S^{A_2} & 0 < S < S^*, \\ \exp(A_3 \times S + A_4) & S^* < S < S_{\max}. \end{cases} \tag{20}$$

where A_1, A_2, A_3 and A_4 are regime-specific coefficients. The value of these parameters is given in Appendix D. This formula captures general nonlinear effect of separation on mixing time, providing a compact, empirical relationship that can be calibrated with simulation or experimental data to predict the time required for inkjet droplets to mix completely via diffusion.

D. Effect of Substrate Wettability

Another key factor is the fluid-solid interactions characterised by the substrate wettability. The droplet-substrate interactions thus far in this study are firmly in the hydrophilic regime. To investigate the effect that substrate wettability has, the hysteresis properties from the original simulations ($\theta_A = 70.0°$, $\theta_E = 63.2°$ and $\theta_R = 45.0°$) were increased to $\theta_A = 100.0°$, $\theta_E = 93.2°$ and $\theta_R = 75.0°$. By doing this, the internal and external dynamics of droplets on a slightly hydrophobic substrate can be investigated and compared to the original results.

Figure 12 shows the time taken for the combined droplets to reach a given mixing index value for different lateral separations. The data from the investigation in Section IV C is plotted translucently with triangle markers for comparison. The trends of the hydrophilic and hydrophobic data are similar which suggests Equation (20) holds true for hydrophobic surfaces. Overall, using a weakly hydrophobic substrate has reduced the time required to mix the droplets. For axisymmetric impacts ($S = 0$) there is a reduction in the time taken to reach a given mixing index by 12%–24%. This is also true for impacts in the spread-coalescence regime ($S > 1.612$), where increasing the hydrophobicity of the substrate results in a noticeable improvement in mixing (11%–14%). However, for depositions with non-zero separation in the coalescence-spread regime ($0 < S < 1.612$), the change in mixing times is less than

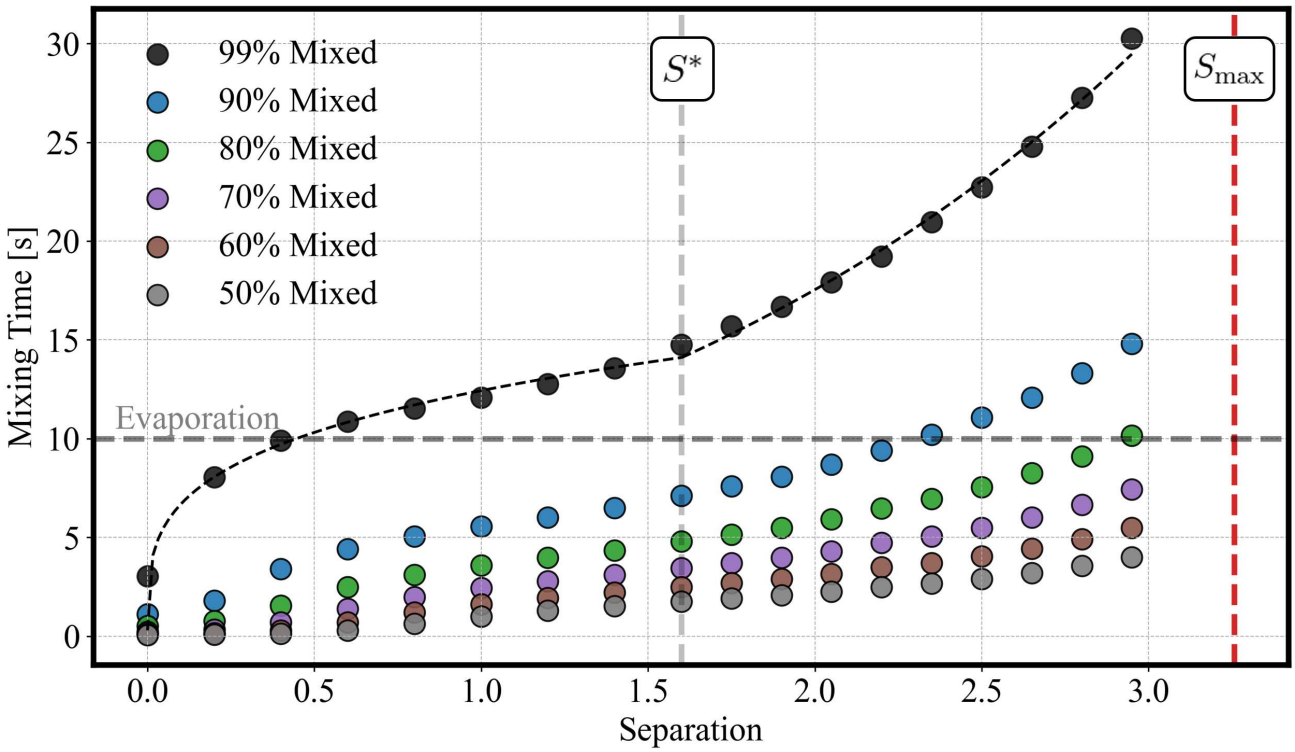

FIG. 11. Mixing time as a function of droplet separation across different mixing thresholds (50% – 99%). Best-fit lines are shown for both the coalescence–spread and spread–coalescence regimes for the 99% data. The timescale in which evaporation becomes important is illustrated by the horizontal dashed line. The red vertical line indicates the maximum feasible separation $S_{\max}$ and the vertical grey line marks the transition point S^*, between the two impact regimes

.

6%. This suggests, for applications printing in the coalescence-spread regime the substrate wettability has little effect on mixing and alternative methods to controlling the printing time are needed. Whereas for applications in the spread-coalescence regime, tuning the substrate wettability could provide a means of enhancing or suppressing mixing.

E. Effect of Droplet Volume

In the investigations carried out thus far, mixing dynamics of two equal volume droplets has been studied. However inkjet printing techniques are used to deposit numerous droplets [42]. As printing continues, the volume of the sessile droplet increases. Hence, it is beneficial to explore the mixing dynamics of printed droplets with a size difference. The size difference between the impacting and sessile droplet can be characterised by the ratio $V_R = V_I/V_S$, of the impacting droplet volume (V_I) to the sessile droplet volume (V_S).

Figure 13(a) shows a volume ratio of $V_R = 0.0008$. In this case, the impact inertia is too small to cause any significant deformation of the sessile droplet. The sessile droplet does not spread over the substrate and the impacting droplet lodges itself on the top of the sessile droplet. When the impacting droplet is smaller than the sessile drop, a curved internal interface between the dyed fluid is created. This contrasts with volume ratios that are close to one, in which a flat internal interface in seen between the dyed fluid, such as in Figure 13(b).

Figure 13(c), presents the case in which the impacting droplet is larger than the sessile droplet $V_R = 2.744$. The inertia of the impacting droplet is now sufficient to cause it to overflow the spreading sessile droplet. At 5 µs, fluid near the spreading contact line of the combined droplet is dyed indicating that during impact, fluid from the impacting droplet has been pushed ahead of the spreading sessile droplet. A very small amount of advective mixing is present in this case near the contact line. The internal interface has been folded on itself and stretched by the spreading of the droplet on the substrate. After 300 µs, the internal interface of the dye is wrapped completely around the undyed

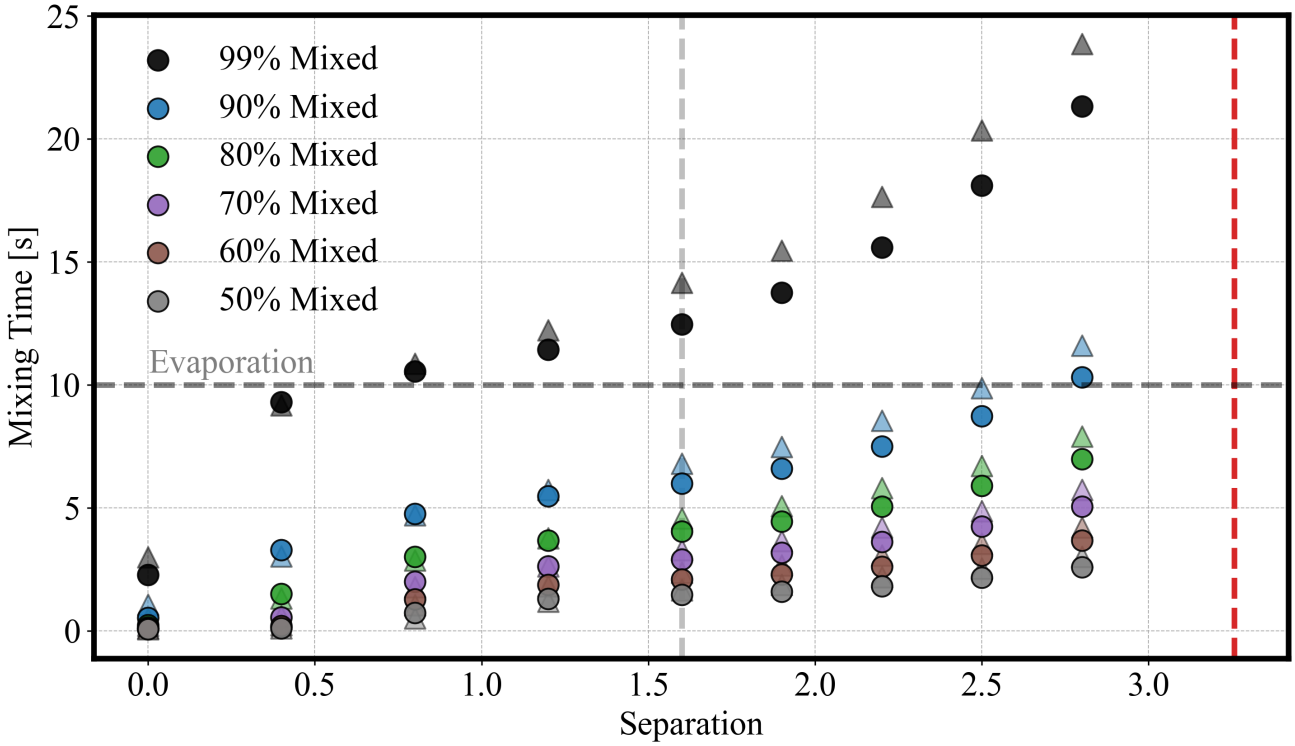

FIG. 12. Time taken for droplets on different substrates to reach a given percentage mixed as a function of droplet separation. Translucent triangle marker results indicate droplets printed on a hydrophilic substrate and opaque results indicate droplets printed on a weakly hydrophobic substrate. The red vertical line indicates the maximum feasible separation $S_{\max}$ and the vertical grey line marks the transition point S^*, between the two impact regimes

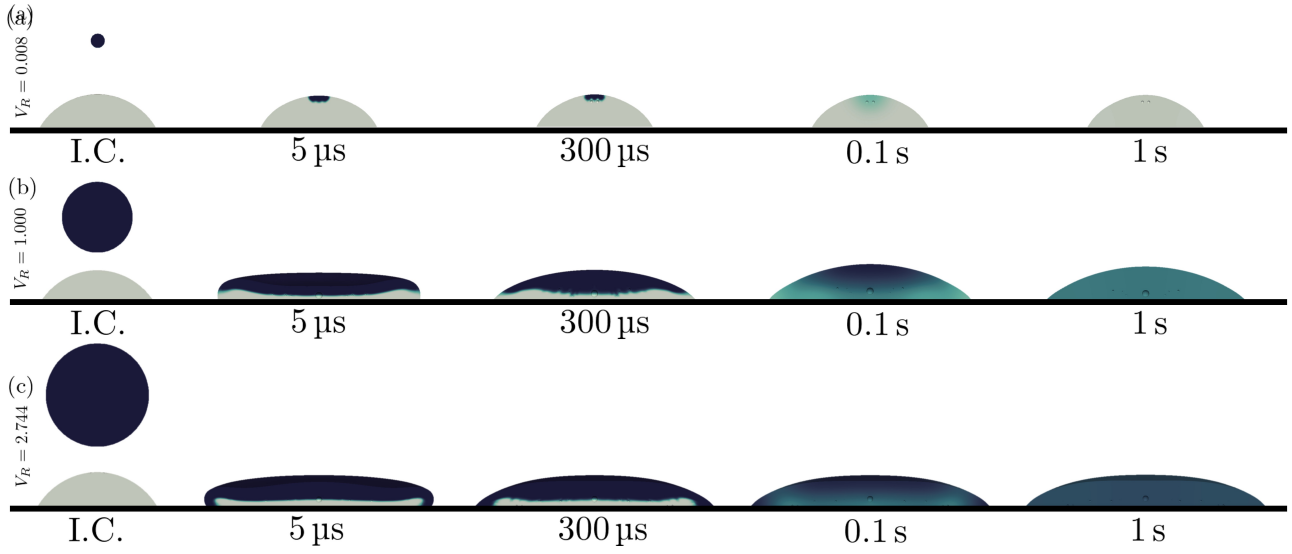

FIG. 13. The internal and external dynamics of printed droplets with various volume ratios between the sessile and impacting droplet. (a) $V_R = 0.008$, (b) $V_R = 1.000$ and (c) $V_R = 2.744$.

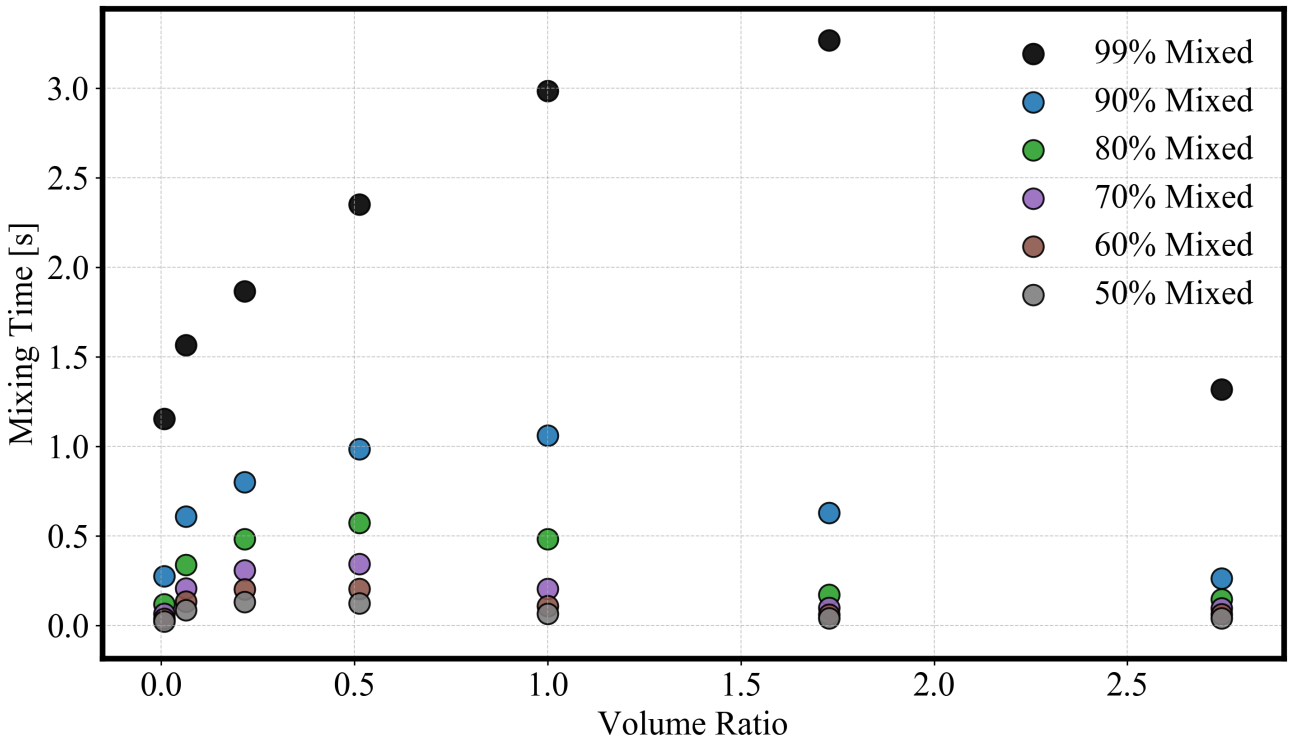

FIG. 14. Comparison of the time taken to reach a given percentage mixed for varying printed droplet volume ratio. There is non-monotonic relationship between amount of mixing and the volume ratio. For very large or very small impacting droplets mixing is the quickest.

fluid further increasing the area in which diffusion can act through in the droplet.

Figure 14 shows the time required for each simulation to reach a given mixing index thresholds. This reveals a complex relationship between droplet mixing and volume ratio. However, across all thresholds, a consistent trend emerges. The mixing time increases with volume ratio, reaches a peak, and then decreases. The complexity of this behaviour is compounded by the fact that the maximum mixing time does not occur at the same volume ratio for each threshold. In particular, transitional behaviours such as the threshold at which the impacting droplet's inertia becomes sufficient to drive spreading across the substrate, or the onset of overspilling, appear to introduce discontinuities or regime changes in the mixing response. These findings suggest that droplet volume ratio is a particularly sensitive and influential parameter in governing mixing dynamics. Even small changes in droplet volume can significantly alter how and where mixing occurs. As such, droplet volume must be carefully considered and potentially fine-tuned in applications where controlled mixing is critical.

V. CONCLUSIONS

The diffusive mixing dynamics of inkjet printed droplets has been explored by considering the system of an impacting and sessile droplet of the same fluid. The internal and external dynamics were successfully simulated using a custom-built numerical model using the OpenFOAM CFD toolbox. Numerical results were validated against previously published and novel laboratory experiments. The coupled model for the transport of a diffusing species within the droplet phase allowed for the qualitative and quantitative assessment of mixing. Overall, simulations showed that, at the scale of typical inkjet applications, diffusive mixing takes place within seconds. This has interesting implications when the evaporative timescales are similar to the diffusive timescales of these systems. Numerical simulations revealed that droplets deposited side-by-side take up to an order of magnitude longer to mix than droplets deposited on-top of one another. The wettability of the substrate had a greater effect on mixing when droplets are deposited with a large separation. In these cases up to 24% quicker mixing occurred. Varying the size ratio between the printed droplets resulted in a highly non-linear change to the mixing within the combined droplet. Both low and high volume ratios

TABLE I. Meshes used in the mesh independence analysis. Refined cells, gives the number of mesh cells within the refined regions of the droplet bulk and free surface. Base cells in the unrefined gas bulk region. Mesh resolutions are calculated with $R_f = 50\,\mu m$.

No. Base Cells per R_f	Refinement Level	No. Refined Cells per R_f	Gas Resolution (µm)	Droplet Resolution (nm)
4	4	64	12.50	781.25
8	3	64	6.25	781.25
10	3	80	5.00	625.00
6	4	96	8.33	520.83
12	3	96	4.17	520.83

experienced quicker mixing than droplets of similar size. These results provide an accurate characterisation of the timescales of diffusive mixing for inkjet printed droplets. This allows the derivation of simple scaling relations that can be used to estimate, design and optimise droplet mixing in a number of relevant applications. Understanding the coupling between key printing parameters and mixing time may enable better control of material synthesis or image resolution in deposition based manufacturing techniques. The parameters investigate here provide a means to tune droplet mixing in a variety of ways to created the desired printing outcome, before other physical effects such as evaporation or drying become important.

ACKNOWLEDGMENTS

This work was supported by the Engineering and Physical Sciences Research Council (EPSRC) Centre for Doctoral Training in Fluid Dynamics at the University of Leeds, grant number EP/S022732/1. Simulations were undertaken on ARC4 and AIRE, which are part of the Advanced Research Computing facilities t the University of Leeds, U.K.

DATA AVAILABILITY

The data that support the findings of this study were generated by numerical simulations. The source code and parameters used to generate the simulations is publicly available [53].

Appendix A: Mesh Sensitivity

A mesh-independence study was performed to ensure that the chosen resolution is sufficient to accurately capture the droplet interface evolution and contact-line dynamics. In order to do this, five meshes with different refinements within the droplet and gas phases have been considered. The meshes are categorised by the number of cells per droplet radius in the gas and droplet regions respectively. Table I shows the details of the meshes used in the mesh sensitivity analysis.

An example explanation of a mesh is as follows. A mesh with 10 cells per R_f and three levels of refinement (which is the typical mesh used in this work) has $10 \times 2^3 = 80$ cells per R_f within the whole droplet phase.

The evolution of the normalised spread length and droplet height is presented in Figure 15 and 16 respectively. Note that the spread length and droplet height are both normalised by their respective initial value. There is little qualitative difference between the meshes examined in this study. However, the lower resolution meshes show a differences to the higher resolution meshes which results in a 1% difference in the final predicted spread length value. The difference is likely due to the complex nature of accurately capturing the moving contact line of the combined droplet. Despite this small difference the meshes are deemed to be insensitive to the resolution in the droplet and gas phases. In this work, 80 cells per R_f were used in the droplet phases, with a base resolution of at least 10 cells per R_f in the gas will be used for all simulations unless stated otherwise. The results of this mesh is denoted by the black circle markers in Figure 15 and Figure 16. The sensitivity analysis undertaken confirms that the free surface and contact line features are sufficiently resolved with this mesh and indeed further refinement unnecessary.

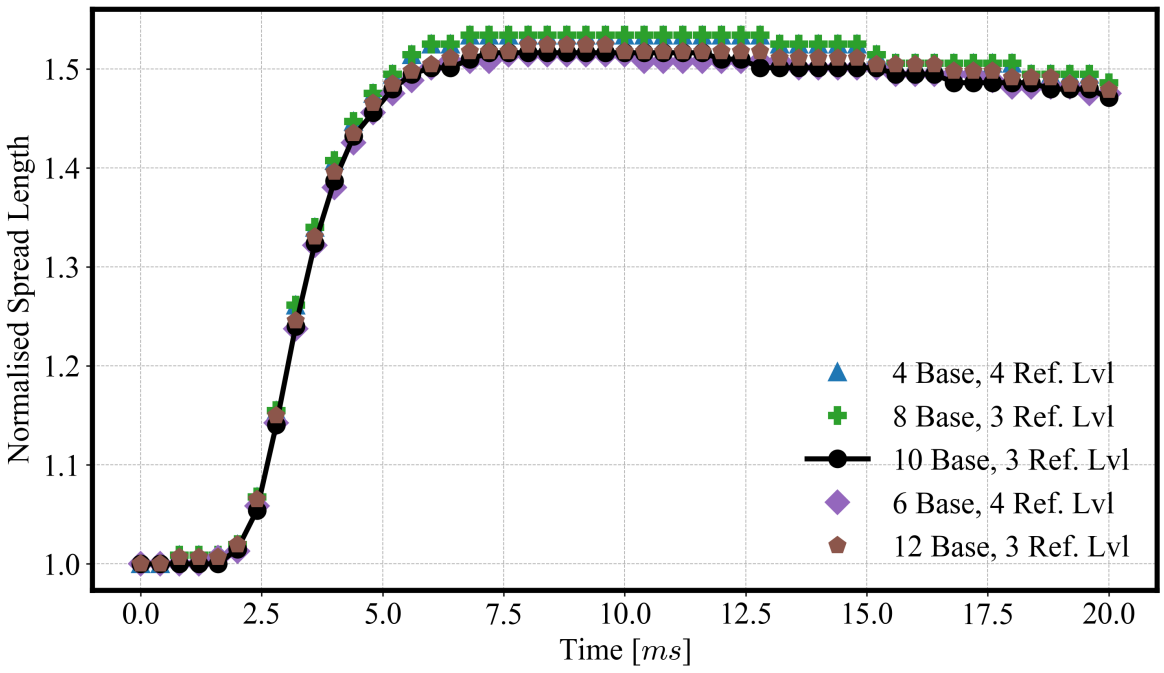

FIG. 15. Evolution of the spread length (normalised by its initial value) for the meshes used in the mesh independence study. The case simulated is the axisymmetric impact and coalescence of a free droplet and sessile droplet on a solid surface. The black circle markers with a line represent the mesh used throughout this work.

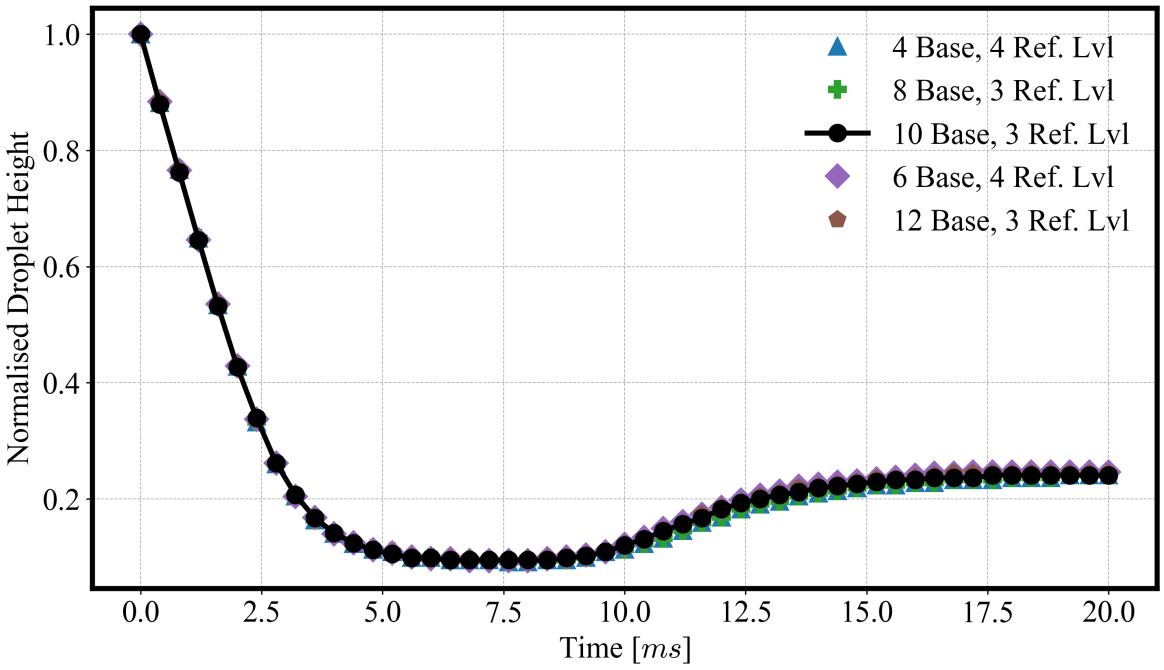

FIG. 16. Evolution of the droplet height (normalised by its initial value) for the meshes used in the mesh independence study. The case simulated is the axisymmetric impact and coalescence of a free droplet and sessile droplet on a solid surface. The black circle markers with a line represent the mesh used throughout this work.

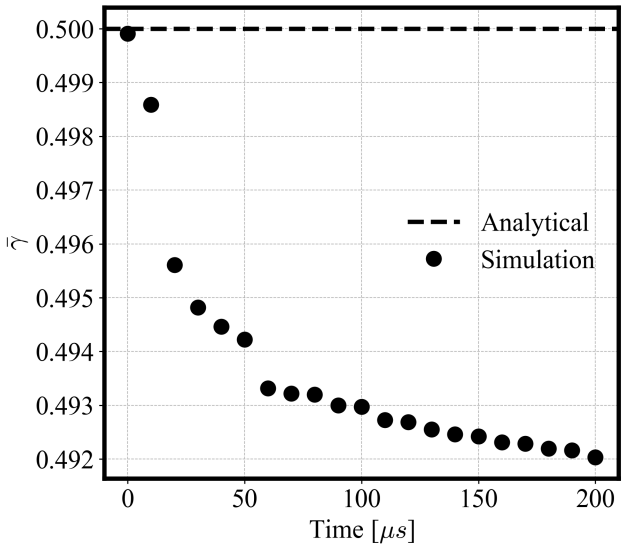

FIG. 17. Evolution of the average value of the diffusing species ($\bar{\gamma}$) over the axisymmetric impact and coalescence of two droplets. The small change in the value of $\bar{\gamma}$ confirms there is good conservation of the scalar γ despite the diffuse representation of the droplet-air free surface.

Appendix B: Conservation of the Diffusing Species

The conservation of the diffusing species within the droplet phase is of paramount importance in ensuring the accuracy of the simulations. The implicit method used to represent the free surface is prone to artificial and unphysical transport over the material interface. Hence it is important to check the diffusing species, represented by the scalar field γ, is conserved within the droplet phase of the simulations. In order to do this, the mean value of the diffusing species $\bar{\gamma}$, was calculated through the simulation of an axisymmetric impact of a free droplet with a sessile droplet presented in Figure 6. This simulation provides a realistic droplet system and timescales that is explored throughout the study. In this system the droplets are initialised to have the same volume, hence a simple conservation argument can be used to derive the exact analytical value of $\bar{\gamma}$ throughout the simulation. The analytical and simulation values of $\bar{\gamma}$ for this system are presented in Figure 17. In this simulation the percentage change to the mean value of γ is 1.6%. Since in two realistic droplet simulations over the typical time scales of interest the change in the value of $\bar{\gamma}$ is calculated to be less than 2%, the method is thought to conserve the diffusing species very well considering the diffuse nature of the free surface.

Appendix C: Static Equilibrium

To quantitatively confirm that the combined droplet had a reached static equilibrium after impact and coalescence, the mean velocity of both the droplet bulk and its free surface was monitored throughout the simulation. Figure 18 illustrates the temporal evolution of these mean velocities. At early times, as the droplets impact and spread on the substrate, the velocity decreases due to viscous dissipation. Around 60 µs, the mean velocity reaches a local minimum, corresponding to the point of maximum spreading, where the droplet has zero kinetic energy. At this stage, the kinetic energy has either been dissipated or converted into surface energy associated with the stretched free surface.

Following this, excess surface energy drives droplet retraction and recoil, causing the mean velocity to increase. The recoil motion is again damped by viscous dissipation, and the droplet gradually slows as it approaches static equilibrium. The velocity associated with the zero-kinetic-energy state at maximum spread provides a useful reference for identifying when the droplet can be considered static, this is indicated by the dashed horizontal line in Figure 18. By approximately 150 µs, both bulk and free surface velocities have decayed below this value, though they both remain comparable. From 180 µs onward, the free surface velocity levels off while the bulk velocity continues to decay.

At this stage, with no excess surface energy remaining in the system, the droplet can be considered at static equilibrium. The non-zero plateau in free surface velocity observed at later times is attributed to parasitic currents

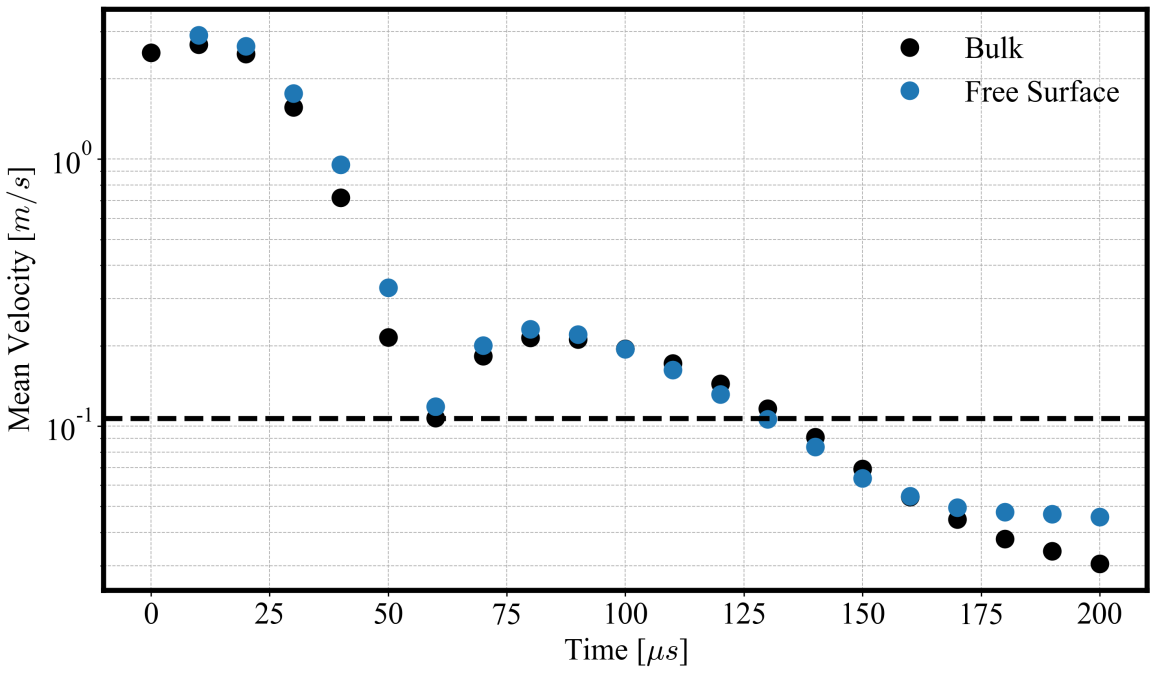

FIG. 18. Evolution of the mean velocity of the bulk and free surface of the combined droplet over the course of the transient numerical simulation. The droplets undergo impact, spread and recoil on the substrate before coming to a static equilibrium. The horizontal dashed line represents the approximate velocity below which the droplet is static.

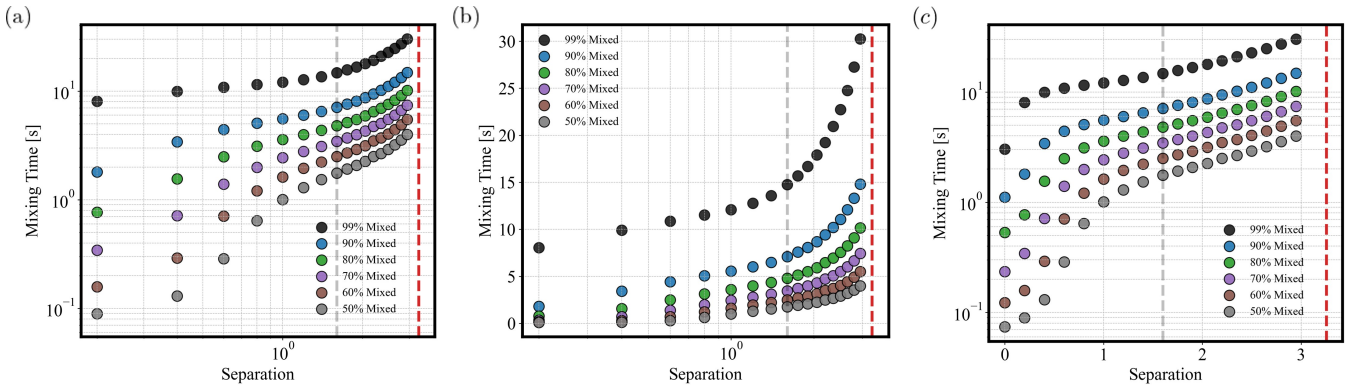

FIG. 19. Separation investigation mixing data plotted on different axes. (a) Both axes are logarithmic. (b) Logarithmic x-axis only. (c) Logarithmic y-axis only. For the 99% mixing threshold a power-law relationship in the coalescence-spread and an exponential relationship in the spread-coalescence regime can be fitted.

inherent to the VOF method. Since the bulk velocity falls below this parasitic scale and the zero-kinetic-energy velocity, the simulation is deemed to have reached equilibrium, beyond which only diffusive transport within the droplet needs to be considered. This equilibrium time was therefore used as the cutoff point for subsequent analyses. This process of conducting a fully dynamic simulation until the droplets reach an static equilibrium is undertaken for all investigations in this study.

Appendix D: Empirical Mixing Time Relationship

To determine an empirical relationship between mixing time, droplet separation, and mixing threshold, the data was plotted on a variety of logarithmic axes (see Figure 19). The data shows a high complex and non-linear relationship between the mixing time, separation and mixing threshold. Determining a robust scaling relationship for this data is out of the scope for this work, however of practical importance is an upper bound for the time needed for inkjet droplets to mix via diffusion.

The time taken for the droplets to become 99% mixed provides an estimate for the upper bound of droplet mixing. Figure 19(a) shows that in the coalescence-spread regime there is a power-law relationship between mixing time and separation as the data is approximately linear on the log-log axes. In the spread-coalescence regime the linear trend on the logarithmic y-axis plot (Figure 19(c)) shows there is an exponential relationship between separation and mixing time.

Hence, an empirical bound for the time needed, T_M, for printed inkjet droplets to mix via diffusion can be stated as

$$T_M = \begin{cases} A_1 S^{A_2} & 0 < S < S^*, \\ \exp(A_3 S + A_4) & S^* < S < S_{\max}, \end{cases}$$

where A_1, A_2, A_3 and A_4 can be obtain from linear regression. Undertaking this curve fitting approach with the data gathered Section IV C yields

$$T_M = \begin{cases} 12.4 \times S^{0.269} & 0 < S < S^*, \\ \exp(0.546 \times S + 1.77) & S^* < S < S_{\max}. \end{cases}$$

[1] H. Sirringhaus, T. Kawase, R. Friend, T. Shimoda, M. Inbasekaran, W. Wu, and E. Woo, "High-resolution inkjet printing of all-polymer transistor circuits," Science **290**, 2123–2126 (2000).

[2] M. Sellier and E. Trelluyer, "Modeling the coalescence of sessile droplets," Biomicrofluidics **3**, 022412 (2009).

[3] H. Song, H.-W. Li, M. S. Munson, T. G. Van Ha, and R. F. Ismagilov, "On-chip titration of an anticoagulant argatroban and determination of the clotting time within whole blood or plasma using a plug-based microfluidic system," Analytical Chemistry **78**, 4839–4849 (2006).

[4] R. E. Saunders, J. E. Gough, and B. Derby, "Delivery of human fibroblast cells by piezoelectric drop-on-demand inkjet printing," Biomaterials **29**, 193–203 (2008).

[5] X. Yang, V. H. Chhasatia, J. Shah, and Y. Sun, "Coalescence, evaporation and particle deposition of consecutively printed colloidal drops," Soft Matter **8**, 9205–9213 (2012).

[6] A. L. Yarin, "Drop impact dynamics: Splashing, spreading, receding, bouncing," Annu. Rev. Fluid Mech. **38**, 159–192 (2006).

[7] C. Josserand and S. T. Thoroddsen, "Drop impact on a solid surface," Annual Review of Fluid Mechanics **48**, 365–391 (2016).

[8] A. Menchaca-Rocha, A. Martínez-Dávalos, R. Nunez, S. Popinet, and S. Zaleski, "Coalescence of liquid drops by surface tension," Physical Review E **63**, 046309 (2001).

[9] N. D. Pawar, S. S. Bahga, S. R. Kale, and S. Kondaraju, "Symmetric and asymmetric coalescence of droplets on a solid surface in the inertia-dominated regime," Physics of Fluids **31** (2019).

[10] R. Li, N. Ashgriz, S. Chandra, J. R. Andrews, and S. Drappel, "Coalescence of two droplets impacting a solid surface," Experiments in Fluids **48**, 1025–1035 (2010).

[11] M. Abdelgawad and A. R. Wheeler, "The digital revolution: a new paradigm for microfluidics," Advanced Materials **21**, 920–925 (2009).

[12] J. R. Castrejon-Pita, E. Betton, K. Kubiak, M. Wilson, and I. Hutchings, "The dynamics of the impact and coalescence of droplets on a solid surface," Biomicrofluidics **5**, 014112 (2011).

[13] S.-I. Yeh, H.-J. Sheen, and J.-T. Yang, "Chemical reaction and mixing inside a coalesced droplet after a head-on collision," Microfluidics and Nanofluidics **18**, 1355–1363 (2015).

[14] Y.-H. Lai, M.-H. Hsu, and J.-T. Yang, "Enhanced mixing of droplets during coalescence on a surface with a wettability gradient," Lab on a Chip **10**, 3149–3156 (2010).

[15] P. Kröber, J. T. Delaney, J. Perelaer, and U. S. Schubert, "Reactive inkjet printing of polyurethanes," Journal of Materials Chemistry **19**, 5234–5238 (2009).

[16] S. Fathi and P. Dickens, "Challenges in drop-on-drop deposition of reactive molten nylon materials for additive manufacturing," Journal of Materials Processing Technology **213**, 84–93 (2013).

[17] J. Castrejón-Pita, K. Kubiak, A. Castrejón-Pita, M. Wilson, and I. Hutchings, "Mixing and internal dynamics of droplets impacting and coalescing on a solid surface," Physical Review E **88**, 023023 (2013).

[18] M. Versluis, "High-speed imaging in fluids," Experiments in Fluids **54**, 1–35 (2013).
[19] V. Cristini and Y.-C. Tan, "Theory and numerical simulation of droplet dynamics in complex flows—a review," Lab on a Chip **4**, 257–264 (2004).
[20] S. Zhao, A. Riaud, G. Luo, Y. Jin, and Y. Cheng, "Simulation of liquid mixing inside micro-droplets by a lattice boltzmann method," Chemical Engineering Science **131**, 118–128 (2015).
[21] C. Chen, Y. Zhao, J. Wang, P. Zhu, Y. Tian, M. Xu, L. Wang, and X. Huang, "Passive mixing inside microdroplets," Micromachines **9**, 160 (2018).
[22] T. C. Sykes, D. Harbottle, Z. Khatir, H. M. Thompson, and M. C. Wilson, "Substrate wettability influences internal jet formation and mixing during droplet coalescence," Langmuir **36**, 9596–9607 (2020).
[23] G. Yi, Z. Cai, Z. Gao, and J. Derksen, "Impingement and mixing dynamics of micro-droplets on a solid surface," Chinese Journal of Chemical Engineering **52**, 66–77 (2022).
[24] H. Jasak, "Openfoam: Open source cfd in research and industry," International journal of naval architecture and ocean engineering **1**, 89–94 (2009).
[25] C. W. Hirt and B. D. Nichols, "Volume of fluid (vof) method for the dynamics of free boundaries," Journal of computational physics **39**, 201–225 (1981).
[26] H. G. Weller, G. Tabor, H. Jasak, and C. Fureby, "A tensorial approach to computational continuum mechanics using object-oriented techniques," Computers in Physics **12**, 620–631 (1998).
[27] X. Xia, C. He, D. Yu, J. Zhao, and P. Zhang, "Vortex-ring-induced internal mixing upon the coalescence of initially stationary droplets," Physical Review Fluids **2**, 113607 (2017).
[28] V. S. Sivasankar, D. R. Hines, and S. Das, "Numerical study of the coalescence and mixing of drops of different polymeric materials," Langmuir **38**, 14084–14096 (2022).
[29] J. U. Brackbill, D. B. Kothe, and C. Zemach, "A continuum method for modeling surface tension," Journal of Computational Physics **100**, 335–354 (1992).
[30] S. S. Deshpande, L. Anumolu, and M. F. Trujillo, "Evaluating the performance of the two-phase flow solver interfoam," Computational Science & Discovery **5**, 014016 (2012).
[31] Y. Okagaki, T. Yonomoto, M. Ishigaki, and Y. Hirose, "Numerical study on an interface compression method for the volume of fluid approach," Fluids **6**, 80 (2021).
[32] N. D. Patil, J. Shaikh, A. Sharma, and R. Bhardwaj, "Droplet impact dynamics over a range of capillary numbers and surface wettability: Assessment of moving contact line models and energy budget analysis," Physics of Fluids **34** (2022).
[33] T. Zhang, J. Wu, and X. Lin, "Lateral motion of a solid with a heterogeneous wettability surface driven by impacting droplets," Journal of Fluid Mechanics **946**, A31 (2022).
[34] R. Attarzadeh and A. Dolatabadi, "Coalescence-induced jumping of micro-droplets on heterogeneous superhydrophobic surfaces," Physics of Fluids **29** (2017).
[35] S. F. Kistler, "Hydrodynamics of wetting," Wettability **6**, 311–430 (1993).
[36] A. S. Rattner and S. Garimella, "Simple mechanistically consistent formulation for volume-of-fluid based computations of condensing flows," Journal of Heat Transfer **136**, 071501 (2014).
[37] K. Vontas, M. Andredaki, A. Georgoulas, K. Nikas, and M. Marengo, "Numerical investigation of droplet impact on smooth surfaces with different wettability characteristics: Implementation of a dynamic contact angle treatment in openfoam," Proceedings of ILASS-Europe 2017 , 58–65 (2017).
[38] L. Wang and J. Sun, "Lattice boltzmann modeling for the coalescence between a free droplet in gases and a sessile droplet on wettable substrate with contact angle hysteresis," Proceedings of the Institution of Mechanical Engineers, Part C: Journal of Mechanical Engineering Science **232**, 431–444 (2018).
[39] J.-Y. Qian, X.-J. Li, Z.-X. Gao, and Z.-J. Jin, "Mixing efficiency analysis on droplet formation process in microchannels by numerical methods," Processes **7**, 33 (2019).
[40] M. Madadelahi and A. Shamloo, "Droplet-based flows in serpentine microchannels: Chemical reactions and secondary flows," International Journal of Multiphase Flow **97**, 186–196 (2017).
[41] M. C. Wilson, J. R. Castrejón-Pita, and A. A. Castrejón-Pita, "Droplet mixing," in *Reactive Inkjet Printing* (2017) pp. 38–58.
[42] D. Lohse, "Fundamental fluid dynamics challenges in inkjet printing," Annual review of Fluid Mechanics **54**, 349–382 (2022).
[43] H. Hu and R. G. Larson, "Evaporation of a sessile droplet on a substrate," The Journal of Physical Chemistry B **106**, 1334–1344 (2002).
[44] S. K. Wilson and H.-M. D'ambrosio, "Evaporation of sessile droplets," Annual Review of Fluid Mechanics **55**, 481–509 (2023).
[45] T. Lim, S. Han, J. Chung, J. T. Chung, S. Ko, and C. P. Grigoropoulos, "Experimental study on spreading and evaporation of inkjet printed pico-liter droplet on a heated substrate," International Journal of Heat and Mass Transfer **52**, 431–441 (2009).
[46] N. Thakur and H. Murthy, "Nickel-based inks for inkjet printing: a review on latest trends," American Journal of Materials Science **11**, 20–35 (2021).
[47] S. Chandra and C. Avedisian, "On the collision of a droplet with a solid surface," Proceedings of the Royal Society of London. Series A: Mathematical and Physical Sciences **432**, 13–41 (1991).
[48] B. L. Scheller and D. W. Bousfield, "Newtonian drop impact with a solid surface," AIChE Journal **41**, 1357–1367 (1995).
[49] M. Pasandideh-Fard, Y. Qiao, S. Chandra, and J. Mostaghimi, "Capillary effects during droplet impact on a solid surface," Physics of Fluids **8**, 650–659 (1996).

[50] I. V. Roisman, "Inertia dominated drop collisions. ii. an analytical solution of the navier–stokes equations for a spreading viscous film," Physics of Fluids **21** (2009).
[51] J. B. Lee, N. Laan, K. G. De Bruin, G. Skantzaris, N. Shahidzadeh, D. Derome, J. Carmeliet, and D. Bonn, "Universal rescaling of drop impact on smooth and rough surfaces," Journal of Fluid Mechanics **786**, R4 (2016).
[52] S. Wildeman, C. W. Visser, C. Sun, and D. Lohse, "On the spreading of impacting drops," Journal of Fluid Mechanics **805**, 636–655 (2016).
[53] Y. Darbar, A. S. Ismail, T. C. Sykes, D. Harbottle, H. M. Thompson, and M. C. T. Wilson, "Data and code for: Role of diffusion in mixing inkjet printed droplets," `https://github.com/yatin-darbar/Droplet_Mixing` (2026).